Journal of Materials Chemistry C

Accepted Manuscript

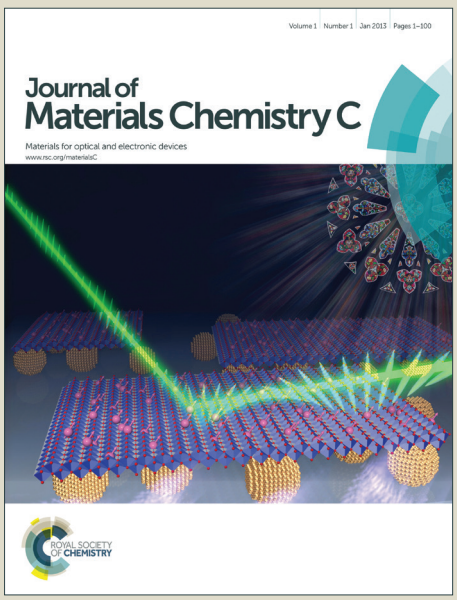

ROYAL SOCIETY OF CHEMISTRY

www.rsc.org/materialsC

Journal of Materials Chemistry C

ARTICLE

Electronic structure, optical and dielectric properties of $BaTiO_3/CaTiO_3/SrTiO_3$ ferroelectric superlattices from first-principles

Received 00th January 20xx,
Accepted 00th January 20xx

DOI: 10.1039/x0xx00000x

www.rsc.org/

Bingcheng Luo [a], Xiaohui Wang [a*], Enke Tian [b], Guowu Li [c], Longtu Li [a*]

The electronic structure, lattice vibrations, optical, dielectric and thermodynamic properties of $BaTiO_3/CaTiO_3/SrTiO_3$ (BT/CT/ST) ferroelectric superlattices are calculated by using first-principles. The lattice parameters after relaxation are in good agreement with the experimental and other theoretical values within error of 1%. The band structure shows an indirect band gap with the value of about 2.039eV, and a direct band gap of 2.39eV at the Γ point. The density of states and the electron charge density along [001] axis are calculated and show the displacement of Ti ions along the [001] axis. The strong hybridization between O 2p and Ti 3d contributes to the ferroelectricity of BT/CT/ST ferroelectric superlattices. The Γ modes are stable, while the vibration modes at A, M, R, and X point are unstable governing the nature of phase transition. The static dielectric tensor including the ionic contribution is calculated and the permittivity parallel to the optical axis is almost eight times more than the permittivity vertical the axis, exhibiting the strong anisotropy. The thermodynamic enthalpy, free energy, entropy, and heat capacity are also investigated based on the phonon properties.

1. Introduction

Ferroelectric materials with ABO_3-type perovskite structure have been extensively studied for their application in sensors, actuators, FRAM memories, capacitors, and energy harvesting and storage devices[1]. Ferroelectric superlattices have received much attention because of their dramatic distinct electric properties from the bulk materials, such as dielectric constant, polarization, Curie temperature, domain and tunability [2-3]. Recently, much research in the ferroelectric superlattices has been focused on the several two-component superlattices, such as $BaTiO_3/SrTiO_3$ [2–4], $KTaO_3/KNbO_3$ [5], $PbTiO_3/PbZrO_3$ [6], $SrTiO_3/NaNbO_3$ [7] and $PbTiO_3/SrTiO_3$ [8,9]. Furthermore, few three-component ferroelectric superlattices, such as $CaTiO_3/BaTiO_3/SrTiO_3$[10], $LaTiO_3/SrTiO_3/YTiO_3$[11], have also been studied theoretically and experimentally.

$BaTiO_3$ was discovered during World War II in 1941 and 1944 in the United States, Russia, and Japan, and found ferroelectric behaviour in 1945 and 1946, and recently paid attention again for the lead-free ferroelectric material which has a successive ferroelectric transition with the temperature reducing[12,13]. It has a cubic perovskite structure with no net polarization which transforms to tetragonal phase with a polarization along the [100] direction at 120℃. Then it transforms to the orthorhombic and rhombohedral phase with the polarization along [111] and [110] direction at -5℃ and -90℃, respectively. The polarization is mainly caused by the displacement of Ti^{4+} cation from the [TiO_6] octahedron center to an off-center position. $SrTiO_3$ is a well-known perovskite material for the quantum paraelectricity which has a very large dielectric constant with the saturation at ε=20000, associated with the softening of a long-wave length transverse optic phonon mode[14]. It can remains paraelectric until the temperature is below 0.3K, while the ferroelectric polarization could easily occurred with the balance of forces broken by the slight perturbation in the lattice structure, such as doping, strain and oxygen isotope substitution [15]. $CaTiO_3$ is also a well-known incipient ferroelectric with a dielectric constant of ε=180 in bulk crystal[16], which shows no ferroelectric phase transition in spite of the intriguing dielectric constant behavior[17]. Contrast to $SrTiO_3$, the paraelectric phase of $CaTiO_3$ is much more difficult to be destroyed by the slight perturbation. The difference in dielectric permittivity of $CaTiO_3$ compared to $SrTiO_3$ is caused by the tilted [TiO_6] octahedrons, which prevent any long-range coupling to neighbouring unit cells[18].

Ferroelectric thin films and the superlattices of these materials with other ABO_3-type perovskite compound have exhibited the enhancement in the dielectric, piezoelectric, and ferroelectric properties. The remanent polarization was enhanced in epitaxial asymmetric $BaTiO_3/SrTiO_3$ strained superlattices, which was ascribed to the increase of lattice parameter *c* of the $BaTiO_3$ layer due to interface strain as well as the increase in the proportion of $BaTiO_3$ [2]. Neaton and Rabe used the first-principles density-functional theory within the local density approximation to study the spontaneous polarization of epitaxial $BaTiO_3/SrTiO_3$ superlattices as a function of composition, revealing the theoretical evidence for the enhancement in the computed superlattice polarization above that of bulk $BaTiO_3$ for superlattices with $BaTiO_3$ fraction

[a] State Key Laboratory of New Ceramics and Fine Processing, School of Materials Science and Engineering, Tsinghua University, Beijing 100084, PR China.
[b] School of Science, China University of Geosciences, Beijing 100083, PR China.
[c] Crystal structure laboratory, National Laboratory of Mineral Materials, China University of Geosciences, Beijing 100083, PR China.

larger than 40%[3]. Epitaxial strain plays an important role in the physical properties of artificial superlattice structures.[19]. Ortega et al presented a way to control the local stress in epitaxial films by altering the lattice parameter by doping and had grown the $BaTiO_3$/(Ba,Sr)TiO_3 ferroelectric superlattices[19]. Meyer and Vanderbilt studied the cubic perovskite compounds with the form $\left(A_{1/3}A'_{1/3}A''_{1/3}\right)BO_3$ and $A\left(B_{1/3}B'_{1/3}B''_{1/3}\right)O_3$ using first-principles methods, and found the strong variation of the strength of the symmetry breaking with the strength of the compositional perturbation[20]. Lee et al fabricated the three-component ferroelectric $BaTiO_3$/$CaTiO_3$/$SrTiO_3$ (BT/CT/ST) superlattices using pulsed laser deposition method, and revealed the subtle effects of a non-inversion-symmetric environment and the role of a large number of coupled heterointerfaces, and verified the theoretical predictions of strain-enhanced ferroelectric polarization of $BaTiO_3$.[10] However, the research that focused on the three-component superlattices is quite few, especially the three-component BT/CT/ST superlattices. Shah et al studied the short-period three-component $SrTiO_3$/$BaTiO_3$/$PbTiO_3$ (ST/BT/PT) perovskite superlattice using first-principles density functional approach.[21] Nakhmanson studied the composition-dependent structural and polar properties of epitaxial short-period BT/CT/ST superlattices grown on a $SrTiO_3$ substrate using first-principles methods.[22] The presence of highly polar CT and BT layers induced substantial polarization and the polarization in the $(ST)_2(BT)_m(CT)_2$ superlattices started to decrease at m=7, indicating the strongest polarization enhancement can be tuned by the delicate balance between concentration and layer thickness.[10,22] Experimentally, Liu et al[23] also showed that the dielectric constant and dielectric loss of the $BaTiO_3$/$SrTiO_3$/MgO superlattices were highly dependent upon the stacking period numbers and layer thicknesses, and the strong interface effect were found in the heterostructures with the combination period larger than 16 or each STO layer less than 6.0 nm.[23,24] Similarly, the dielectric constant, dielectric loss, and tunabilities of the Mn:BST/Mn:BZT/MgO heterostructures are highly dependent upon the sequences of Mn:BST to Mn:BZT.[25] Obviously, Nakhmanson only focused the polarization enhancement while Gao only concentrated on the intrinsic asymmetric ferroelectricity together with the heterostructure between metal and ferroelectric superlattices. But the band structure, elastic properties, optical dielectric function, lattice vibration, and thermodynamics properties of BT/CT/ST ferroelectric superlattices are still not reported. Thus, in this work, we perform first-principles calculations to study the properties of BT/CT/ST ferroelectric superlattices. The structural, electronic, optical properties are investigated using standard density functional theory. The lattice vibrations and thermodynamics properties are analyzed with the density functional perturbation theory.

2. Method and computational details

The first-principle calculations were performed by employing the pseudopotential plane-wave (PP-PW) approach based on the density functional theory (DFT) framework as implemented in the Cambridge Serial Total Energy (CASTEP) code[26]. The generalized gradient approximation (GGA) with the PBE exchange-correlation functional was used. The norm-conserving pseudopotentials adopted for the ferroelectric superlattices were constructed by the electron configurations as Ca $3s^23p^64s^2$ states, Sr $4s^24p^65s^2$ states, Ba $5s^25p^66s^2$ states, Ti $3s^23p^63d^24s^2$ states, and O $2s^22p^4$ states. The structure was fully relaxed with a 6×6×1 special k-point mesh grid and 880 eV energy cutoff for the plane-wave basis, which had been carefully tested to ensure the well-converged total energy and geometrical configurations[27]. The energy tolerance was 5×10^{-6} eV/atom, the force tolerance was 0.01 eV/Å, and the stress tolerance is 0.02GPa, and the displacement tolerance was 5×10^{-4} Å. Then the band structure, density of states, electron density, and optical properties were calculated. In order to strengthen the validation of calculation, we also used VASP code to relax the structure and calculate the properties[28,29]. The phonon, dielectric and thermodynamic properties were calculated by using the density functional perturbation theory (DFPT) with a linear response method implanted in CASTEP code[30]. Fig. 1 shows the schematic crystal structure of BT/CT/ST ferroelectric superlattices. The BT/CT/ST superlattices with P4mm symmetry were constructed based on the cubic $BaTiO_3$, $SrTiO_3$, and $CaTiO_3$ crystal. The lattice constant of the superlattice is fixed to the bulk cell parameter of bulk $SrTiO_3$, to implicitly include the $SrTiO_3$ substrate[31–33].

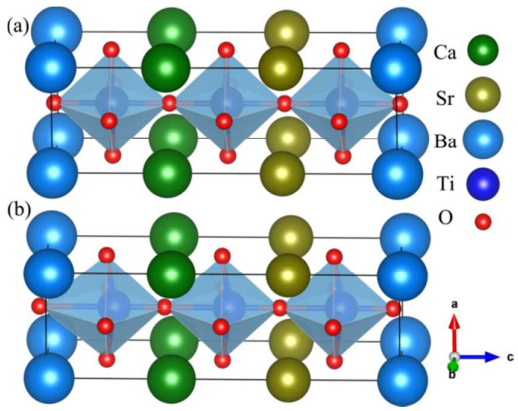

Fig. 1. Schematic crystal structure of BT/CT/ST ferroelectric superlattices before (a) and after (b) relaxation. Pictures drawn with VESTA[34].

3. Results and discussion

3.1. Structural and electronic properties of BT/CT/ST ferroelectric superlattices

We first relaxed the superlattice to obtain the geometry optimized atom configuration. The calculated lattice parameter of BT/CT/ST ferroelectric superlattices are a=b=3.88 Å, c=11.85 Å and the c/a ratio is 3.05, which is in great agreement with the experimental value of 3.02 and other theoretical value of 3.018 [22]. This error within of 1% confirmed the validation and reliability of our methods.

The calculated band structure of BT/CT/ST ferroelectric superlattices is shown in Fig. 1. The Fermi level is fixed to zero at the top of valence band. The maximum of valence band and minimum of conduction band are located at A point and Γ point, respectively, which indicates the BT/CT/ST ferroelectric superlattices are an indirect band gap materials with the value of about 2.039eV. It is also clear that the smallest direct band gap is 2.39eV at the Γ point. Our results are in consistency with

the band gap of 2.3 eV according to Gao et al,[32] but they didn't show the band structure. Considering that there is no detailed report about the experimental band gap, we compared with the gaps of $BaTiO_3$, $CaTiO_3$, and $SrTiO_3$. According to the literature[35,36], these three components are indirect band materials, indirectly revealing the rationality of present calculation of band gaps. It is well known that the band gap can be underestimated due to the choice of exchange correlation functional. The total density of states (DOS) and the partial density of states (PDOS) of BT/CT/ST ferroelectric superlattices are shown in Fig. 3 information in the energy region nearer the Fermi level. It can be seen that the valence band from -6~0eV mainly consists of O 2p states, together with small contribution from Ti 3d states. Considering that the partial density of states for the Ba, Sr, and Ca ions is lower than 0.3 electrons per cell, these contributions can be ignored. The conduction band minimum from 0~6eV is mainly originated from Ti 3d states, together with small contribution of O 2p states. The density of Ti 3d is much higher than that of O 2p, indicating that some electrons of O atom move from valence band to conduction band and hybrid with Ti 3d electrons. It can be also seen that the PDOS difference between O 2p states and Ba (also Sr，Ca) states is much larger than that between O 2p states and Ti 3d state, indicating that the Ti-O bonding is covalent and the Ba-O (also Sr-O，Ca-O) bonding is ionic. The strong hybridization between O 2p and Ti 3d contributes to the ferroelectricity of BT/CT/ST ferroelectric superlattices.

To better understand the charge distribution and the nature of the chemical bonding, the electron charge density for BT/CT/ST ferroelectric superlattices along [001] axis is calculated and the results are shown in Fig. 4. It can be seen that the charge distribution around Ti site reveals that the bonding between Ti and O is covalent, while the charge distribution around Ba site shows the ionic behavior between Ba and O. Similarly, the bonding between Ca and O and the bonding between Sr and O are also mainly ionic. Furthermore, the interatomic distance between Ti and O1 is 1.773 Å, which is much smaller than the interatomic distance of 2.765Å between Sr and O1, indicating the covalent nature of the Ti-O bonding. It can also be seen that the interatomic distance between Ti and O1 atom is much shorter than the interatomic distance between Ti and O2 atom, indicating the displacement of Ti ions along the [001] axis. This shows the evidence for the ferroelectricity of BT/CT/ST ferroelectric superlattices.

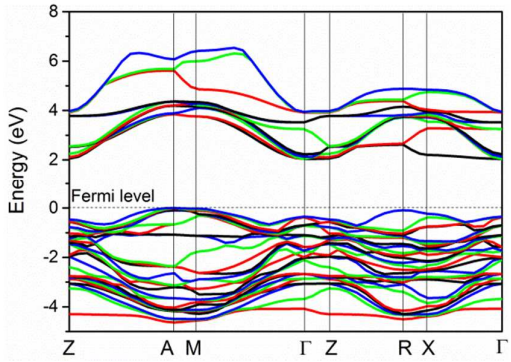

Fig. 2 Band structure of BT/CT/ST ferroelectric superlattices along high-symmetry direction. The Fermi level is located at zero energy, indicated by the horizontal dotted line.

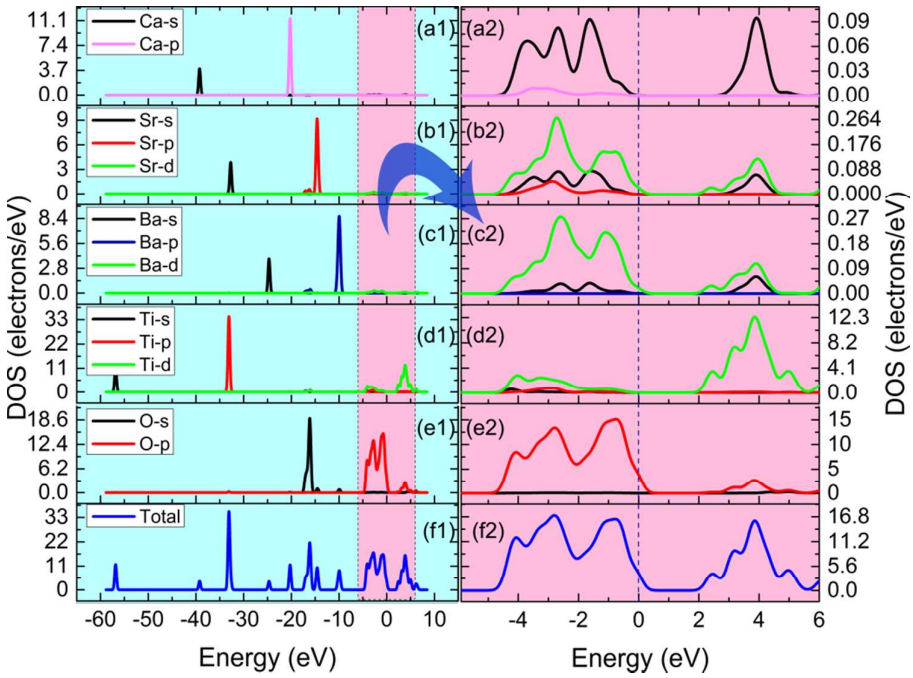

Fig. 3 Total density of states and partial density of states of BT/CT/ST ferroelectric superlattices in the energy range from -8 to 8eV.

Journal of Materials Chemistry C

ARTICLE

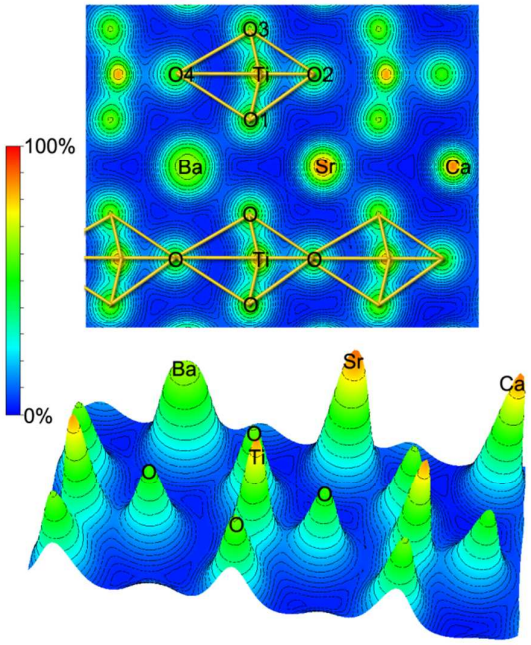

Fig. 4 Electron charge density for BT/CT/ST ferroelectric superlattices along *[001]* axis: (a) in (110) plane; (b) in three dimension. Pictures drawn with VESTA[38].

3.2. Optical properties of BT/CT/ST ferroelectric superlattices

The optical properties of BT/CT/ST ferroelectric superlattices can be calculated from the complex dielectric function

$$\varepsilon(\omega)=\varepsilon_1(\omega)+i\varepsilon_2(\omega) \tag{1}$$

where ε_1 and ε_2 are the real part and the imaginary part of the dielectric function, respectively. The imaginary part of dielectric function is dependent on the frequency and can be calculated by[37]

$$\varepsilon_2(\omega)=\frac{2\pi e^2}{\Omega\varepsilon_0}\sum_{\mathbf{k},v,c}\left|\left\langle\Psi_{\mathbf{k}}^{c}\left|\mathbf{u}\cdot\mathbf{r}\right|\Psi_{\mathbf{k}}^{v}\right\rangle\right|^2\delta\left(E_{\mathbf{k}}^{c}-E_{\mathbf{k}}^{v}-\mathrm{h}\omega\right) \tag{2}$$

where ε_0 is the vacuum dielectric constant, Ω is the volume, v and c represents the valence and conduction band, respectively, $\mathrm{h}\omega$ is the energy of the incident phonon, **u** is the vector defining the polarization of the incident electric field, $\mathbf{u}\cdot\mathbf{r}$ is the momentum operator, $\Psi_{\mathbf{k}}^{c}$ and $\Psi_{\mathbf{k}}^{v}$ are the wave function of conduction band and valence band at *k* point, respectively. According to the imaginary part of dielectric function, all optical properties such as refractive index *n(ω)*, extinction coefficient *k(ω)*, absorption coefficient *α(ω)*, reflectivity *R(ω)*, energy loss spectrum *L(ω)*, and the optical conductivity *σ(ω)* can be given by[37,38]

$$n(\omega)=\frac{1}{\sqrt{2}}\left\{\left[\varepsilon_1^2(\omega)+\varepsilon_2^2(\omega)\right]^{\frac{1}{2}}+\varepsilon_1(\omega)\right\}^{\frac{1}{2}} \tag{3}$$

$$k(\omega)=\frac{1}{\sqrt{2}}\left\{\left[\varepsilon_1^2(\omega)+\varepsilon_2^2(\omega)\right]^{\frac{1}{2}}-\varepsilon_1(\omega)\right\}^{\frac{1}{2}} \tag{4}$$

$$\alpha(\omega)=\frac{\sqrt{2}\omega}{c}\left\{\left[\varepsilon_1^2(\omega)+\varepsilon_2^2(\omega)\right]^{\frac{1}{2}}-\varepsilon_1(\omega)\right\}^{\frac{1}{2}} \tag{5}$$

$$R(\omega)=\left|\frac{\sqrt{\varepsilon_1(\omega)+i\varepsilon_2(\omega)}-1}{\sqrt{\varepsilon_1(\omega)+i\varepsilon_2(\omega)}+1}\right|^2 \tag{6}$$

$$L(\omega)=\mathrm{Im}\left(\frac{-1}{\varepsilon(\omega)}\right)=\frac{\varepsilon_2(\omega)}{\varepsilon_1^2(\omega)+i\varepsilon_2^2(\omega)} \tag{7}$$

$$\sigma(\omega)=\sigma_1(\omega)+i\sigma_2(\omega)=-i\frac{\omega}{4\pi}\left[\varepsilon_1(\omega)+i\varepsilon_2(\omega)-1\right] \tag{8}$$

Fig. 5 shows the dielectric function, absorption coefficient, reflectivity, conductivity, refractive index, and electron energy-loss spectrum. From Fig. 5 (a), it can be seen that the peaks for the imaginary part dielectric function at 4.3 eV and 6.7eV is much stronger than other peaks, which is mainly originated from the transition from O 2p valence band to Ti 3d conduction band. The peak at high energy (~20.0eV) arises from the transition from O 2s to the Ti 3d states, while the peak at even much higher energy around 36.9eV should derive from the transition from the Ti 3p level to conduction band, which is consistent with the reflectivity in Fig. 5 (c).These also explains the origin of the peak structures in the refractive index and extinction coefficient spectra as shown in Fig. 5 (c). From the real part of dielectric function in Fig. 5 (a), it can be clearly seen the static dielectric constant is 4.5, which only contains the contributions of electrons. The contributions of ionic vibrations to the dielectric constant will be discussed in the following section. From the real part of the refractive index, the static refractive index is 2.1. This large fractive index in the low energy range exhibiting the high band gap[39], which is in good accordance with the band calculations as shown in Fig. 2 . In the range from 0 to 2.4 eV and above 11eV the reflectivity for BT/CT/ST ferroelectric superlattices is lower than 20%, displaying that BT/CT/ST superlattices are transparent for photons at these ranges. The energy loss function describes the energy lost by an electron passing from a homogeneous dielectric materials, the peaks in the energy loss spectrum locates at 10.7eV, 20.2 eV, and 38.0 eV. The peak at 10.7 eV is high and sharp, indicating the energy loss range is narrow and it is useful for the optical storage efficiency. The main peak is defined as the bulk plasma frequency ω_p, above and below

which the material exhibits dielectric [$\varepsilon_1(\omega)>0$] and metallic [$\varepsilon_1(\omega)<0$] behavior[40]. The sharp structure located at 10.7 eV is related with the sharp decrease in the reflectivity as shown in Fig. 5 (c). This process is associated with the electrons transition from O 2s and Ba 6s, lying below the valence band, to the empty conduction band as shown in Fig. 3.

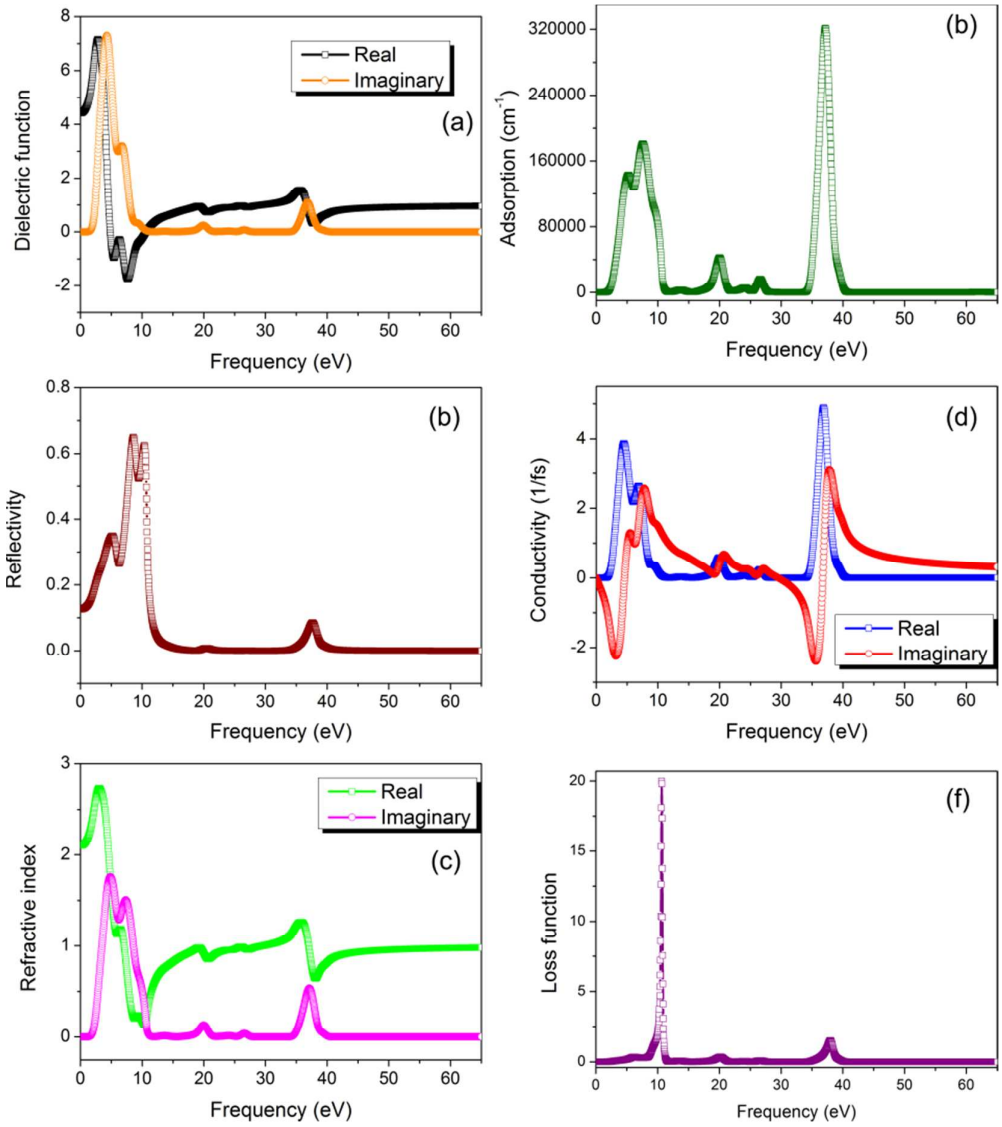

Fig. 5 The dielectric function(a) , absorption coefficient (b), reflectivity (c), conductivity (d),refractive index (e), and electron energy-loss spectrum (f) of BT/CT/ST ferroelectric superlattices

3.3. Lattice vibrations and dielectric properties of BT/CT/ST ferroelectric superlattices

To better understand the lattice dynamics and dielectric properties of BT/CT/ST ferroelectric superlattice, the phonon dispersion curves and phonon density of states are calculated using density functional perturbation theory[30]. According to the literature[41–44], the phonon properties can be obtained using a harmonic approximation by:

$$D_{\mu\nu}\left(\mathbf{R}-\mathbf{R}'\right)=\left.\frac{\partial^2 E}{\partial u_\mu\left(\mathbf{R}\right)\partial u_\nu\left(\mathbf{R}'\right)}\right|_{u=0} \quad (9)$$

where u refers to the displacement of a given atom and E is the total energy in the harmonic approximation. This force constants matrix can be written in reciprocal space and usually referred to as the dynamical matrix:

$$D_{\mu\nu}(\mathbf{q}) = \frac{1}{N_{\mathbf{R}}} \sum_{\mathbf{R}} D_{\mu\nu}(\mathbf{R}) e^{-i\mathbf{qR}} \tag{10}$$

The plane waves are employed to evaluate each atomic displacement:

$$\mathbf{u}(\mathbf{R}, t) = \varepsilon e^{i(\mathbf{qR} - \omega(\mathbf{q})t)} \tag{11}$$

where the polarization vector of each mode, **ε**, is an eigenvector with the dimension of 3N of the eigenvalue problem:

$$M\omega(\mathbf{q})^2 \varepsilon = D(\mathbf{q})\varepsilon \tag{12}$$

The contribution to the partial density of state on atom *i*, from each phonon band, is evaluated using:

$$N_i(E) = \int \frac{d\mathbf{k}}{4\pi^3} \left| e_j(i) \right|^2 \delta\left(E - E_n(\mathbf{k})\right) \tag{13}$$

where e_j is the eigenvector associated with the mode of energy E_j. Considering the tetragonal primitive cell of BT/CT/ST ferroelectric superlattices contains 15 atoms, the complete phonon spectrum consists of 45 normal modes of vibration including 3 acoustical branches and 42 optical branches. Through the standard group theoretical analysis, the phonon modes at Γ point in the Brillouin-zone center can be represented as

$$\Gamma_{vib} = 12A_1 \oplus 3B_1 \oplus 15E \tag{14}$$

where A1, B1 and E are the irreducible representation for the symmetry of lattice vibrations. A1 and E modes are both Raman and Infrared active while B mode is only Raman active. E presentation is two dimensional while A1 and B1 are one dimensional. One A1 mode and one E pair are acoustic, leaving the others optical. The calculated phonon dispersion curves along the high symmetry lines of tetragonal Brillouin zone are shown in Fig. 6, together with the phonon density of states. It is clear that no imaginary frequency is found at Γ point showing stable character. However, there exists imaginary frequency at A, M, R, and X point, whose phonon disperse curves are shown below zero frequency, indicating the unstable modes. These unstable modes govern the nature of phase transition, dielectric and ferroelectric response of BT/CT/ST ferroelectric superlattices. The phonon DOS in the frequency region below 20 THz is mainly contributed by the Ti-O hybridization of [TiO_6] octahedron.

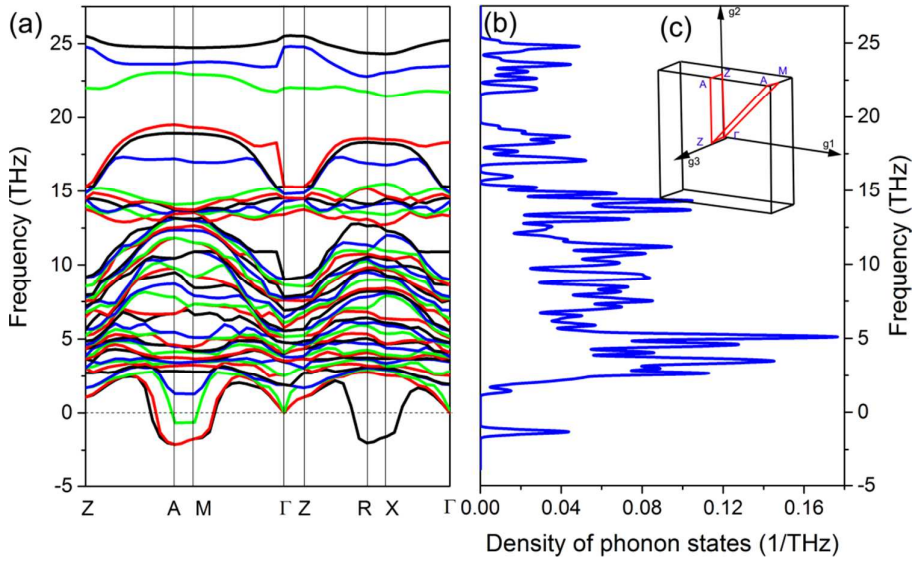

Fig. 6 The calculated phonon dispersion curves (a) along high-symmetry direction (c) and phonon density of states (b) for BT/CT/ST ferroelectric superlattices.

The Born effective charges control the amplitude of the long-range Coulomb interactions between nuclei and the splitting between longitudinal optic (LO) and transverse optic (TO) phonon modes. The Born effective charge tensors $Z^*_{\alpha\beta}$ is defined as the partial derivative of the macroscopic polarization concerning a periodic displacement of all the periodic images of that ion at zero macroscopic electric field[45,46],

$$Z^*_{\alpha\beta}(\kappa) = \Omega_0 \frac{\partial P_\alpha}{\partial \tau_\beta(\kappa)}\bigg|_{\xi=0} = \frac{\partial F_\beta(\kappa)}{\partial} \tag{15}$$

where P_α is the total macroscopic polarization per unit cell generated in the β direction, Ω_0 is the volume of the unit cell, τ is the rigid displacement of the sublattice of κth atom along the α direction. The Born effective charges are calculated through linear response method with density functional perturbation theory, and the diagonal tensors are shown in

Table I, together with the nominal charges. The Born effective charges of all the atoms in ferroelectric superlattices are larger than their nominal ionic values owing to the ions displacement during phase transition, favouring the ferroelectric instability. The large values of Z_{Ti} and Z_O further revealing the strong hybridization between O 2p and Ti 3d states and the dynamic charge transfer along Ti-O bonds, which also explains that the Mulliken charges are lower than the Born effective charges. Combining the ionic contribution to the dielectric properties, the static dielectric tensor is calculated with two different components, $\varepsilon_{\perp}^{0}$ =25.5 and $\varepsilon_{\parallel}^{0}$ =203.4. Obviously the static dielectric permittivity is larger than the optical dielectric permittivity. The static dielectric tensor parallel to the axis is almost eight times more than that vertical the axis, showing the strong anisotropy. The dielectric response along the optical axis is electronic, while that perpendicular the optical axis is ionic. Polarization enhancement with respect to bulk tetragonal $BaTiO_3$ has been reported for two- and three-component superlattices with a BaTiO3 concentration of more than 30%[22]. The concentration and layer thickness of individual layer are identified as an important factor governing the polarization improvement. The polarization of the $(ST)_l(BT)_m(CT)_n$ superlattices increases with the increase of the (CT) layer thickness, while the $(ST)_2(CT)_2$ system is substantially more polar than $(ST)_1(CT)_1$, and $(BT)_2(CT)_2$ is more polar than $(ST)_2(BT)_2$.[22] Gao et al[32] studied the intrinsic asymmetric ferroelectricity of the BT/CT/ST tricolour superlattice at the nanoscale and showed the relationship between the polarization directions and geometric stacking sequences of the superlattices. Similar polarization enhancement has been reported in $(ST)_x(BT)_y(PT)_z$ system, and the lattice distortion in superlattices can be manipulated by changing the layer thicknesses.[21]

Table I The calculated Born effective charge tensors, average of their eigenvalues, nominal charges and Mulliken charges of Ba, Sr, Ca, Ti and O in BT/CT/ST ferroelectric superlattices in unit *e*.

Atoms	Z	λ	Nominal charge	Mulliken charge
Ba	[2.752 2.752 3.013]	2.839	+2	1.53
Sr	[2.518 2.518 3.013]	2.609	+2	1.34
Ca	[2.515 2.515 2.590]	2.540	+2	1.41
Ti1	[6.637 6.637 4.616]	5.963	+4	1.3
Ti2	[6.667 6.667 5.226]	6.187	+4	0.89
Ti3	[6.619 6.619 5.306]	6.181	+4	1.27
O1	[-2.038 -2.038 -4.095]	-2.724	-2	-1.12
O2	[-1.695 -1.695 -4.402]	-2.598	-2	-0.75
O3	[-1.702 -1.702 -4.741]	-2.715	-2	-0.74
O4	[-2.001 -1.768 -5.460]	-3.077	-2	-0.9
O5	[-1.963 -1.700 -5.474]	-3.045	-2	-0.77
O6	[-2.017 -1.685 -5.359]	-3.020	-2	-0.9

3.4. Thermodynamic properties of BT/CT/ST ferroelectric superlattices

With the calculation of phonon properties, the thermodynamic enthalpy H, free energy F and entropy S at finite temperature can be computed. The vibration contribution to the free energy is derived by[47]

$$H(T) = E_{tot} + \frac{1}{2}\int g(\omega)\hbar\omega d\omega + \int \frac{\hbar\omega}{e^{\frac{\hbar\omega}{k_B T}} - 1} g(\omega) d\omega \quad (16)$$

$$F(T) = E_{tot} + \frac{1}{2}\int g(\omega)\hbar\omega d\omega + k_B T \int g(\omega)\ln(1 - e^{\frac{\hbar\omega}{k_B T}}) d\omega \quad (17)$$

$$S(T) = k_B \left[\int \frac{\frac{\hbar\omega}{k_B T}}{e^{\frac{\hbar\omega}{k_B T}} - 1} g(\omega) d\omega - \int g(\omega) \ln\left(1 - e^{\frac{\hbar\omega}{k_B T}}\right) d\omega \right] \quad (18)$$

where $g(\omega)$ is the phonon density of states, k_B is the Boltzmann constant. Fig. 7 shows the Temperature dependence of the calculated thermodynamic enthalpy, free energy, and temperature times entropy for BT/CT/ST ferroelectric superlattices. It is clear that the enthalpy and free energy increase with the temperature increase, while the entropy decreases with the temperature increase. All these three terms in Fig. 7 yields to zero when the temperature approaches zero, which is in accordance with Third law of thermodynamics. Fig. 9 shows the temperature dependence of Debye temperature and heat capacity derived from phonon model for BT/CT/ST ferroelectric superlattices. It can be seen that the heat capacity approaches Dulong–Petit classical limit at high temperature. All these thermodynamic properties can be compared with experimental results and predict the phase stability.

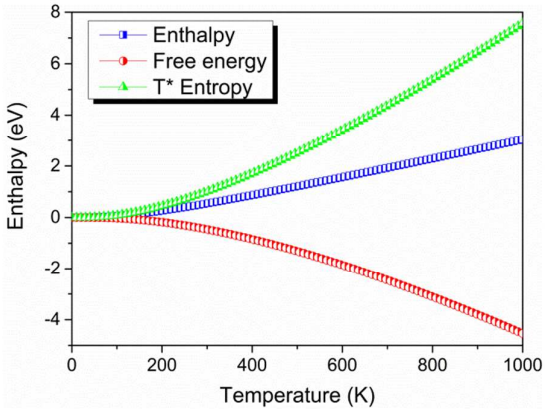

Fig. 7 Temperature dependence of the calculated thermodynamic enthalpy (blue line), free energy (red line), and temperature times entropy (green line) for BT/CT/ST ferroelectric superlattices.

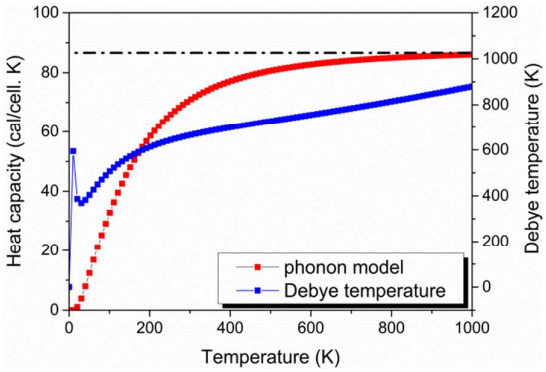

Fig. 8 Temperature dependence of Debye temperature and heat capacity derived from phonon model. The heat capacity approaches Dulong–Petit classical limit at high temperature.

4. Conclusions

In this work, we investigated the electronic structure, lattice vibrations, optical, dielectric and thermodynamic properties of $BaTiO_3/CaTiO_3/SrTiO_3$ ferroelectric superlattices by employing the pseudopotential plane-wave approach based on the density functional theory framework. After relaxation, the lattice parameters are in good agreement with the experimental and other theoretical values within error of 1%. The band structure shows an indirect band gap with the value of about 2.039eV between A and Γ point, and a direct band gap of 2.39eV at the Γ point. The density of states shows that the Ti-O bonding is covalent and the Ba-O (also Sr-O，Ca-O) bonding is ionic. The electron charge density for BT/CT/ST ferroelectric superlattices along [001] axis is calculated and the results show the displacement of Ti ions along the [001] axis. The strong hybridization between O 2p and Ti 3d contributes to the ferroelectricity of BT/CT/ST ferroelectric superlattices. The dielectric function, absorption coefficient, reflectivity, conductivity, refractive index, and electron energy-loss spectrum are also calculated and discussed. The phonon dispersion curves and phonon density of states are calculated using density functional perturbation theory. No imaginary frequency is found at Γ point showing stable character, while the imaginary frequency at A, M, R, and X point indicates unstable modes, which governs the nature of phase transition. Combing the ionic contribution to the dielectric properties, the static dielectric tensor including the ionic contribution is calculated and the permittivity parallel to the optical axis is almost eight times more than the permittivity vertical the axis, exhibiting the strong anisotropy. The thermodynamic enthalpy, free energy, entropy, and heat capacity are also investigated based on the phonon properties. Given that there are few experimental results of BT/CT/ST ferroelectric superlattices reported, especially the optical, phonon, and thermodynamic properties, we hope this predictive first-principles calculations will attract the attention and motivate the experimental investigations.

Acknowledgements

The work was supported by Ministry of Sciences and Technology of China through National Basic Research Program of China (973 Program 2015CB654604), National Natural Science Foundation of China for Creative Research Groups (Grant No.51221291), National Natural Science Foundation of China (Grant No. 51272123), the Fundamental Research Funds for the Central Universities (Grant No.2652013105), and also supported by CBMI Construction Co., Ltd.

Notes and references

1 1Y. Yano, K. Iijima, Y. Daitoh, T. Terashima, Y. Bando, Y. Watanabe, H. Kasatani and H. Terauchi, *J. Appl. Phys.*, 1994, **76**, 7833.
2 2T. Shimuta, O. Nakagawara, T. Makino, S. Arai, H. Tabata and T. Kawai, *J. Appl. Phys.*, 2002, **91**, 2290.
3 J. B. Neaton and K. M. Rabe, *Appl. Phys. Lett.*, 2003, **82**, 1586.
4 W. Tian, J. C. Jiang, X. Q. Pan, J. H. Haeni, Y. L. Li, L. Q. Chen, D. G. Schlom, J. B. Neaton, K. M. Rabe and Q. X. Jia, *Appl. Phys. Lett.*, 2006, **89**, 092905.
5 E. D. Specht, H.-M. Christen, D. P. Norton and L. A. Boatner, *Phys. Rev. Lett.*, 1998, **80**, 4317–4320.
6 C. Bungaro and K. M. Rabe, *Phys. Rev. B*, 2004, **69**, 184101.
7 J. Narkilahti, M. Plekh, J. Levoska and M. Tyunina, *Phys. Rev. B*, 2009, **79**, 14106.
8 M. Dawber, C. Lichtensteiger, M. Cantoni, M. Veithen, P. Ghosez, K. Johnston, K. M. Rabe and J.-M. Triscone, *Phys. Rev. Lett.*, 2005, **95**, 177601.
9 M. Gu, J. Wang, Q. Y. Xie and X. S. Wu, *Phys. Rev. B*, 2010, **82**, 134102.
10 H. N. Lee, H. M. Christen, M. F. Chisholm, C. M. Rouleau and D. H. Lowndes, *Nature*, 2005, **433**, 395–399.
11 M. Kareev, Y. Cao, X. Liu, S. Middey, D. Meyers and J. Chakhalian, *Appl. Phys. Lett.*, 2013, **103**, 231605.
12 B. Wul, *Nature*, 1946, **157**, 808.
13 D. K. and R. M. and G. E. K. and L. Godefroy, *J. Phys. Condens. Matter*, 1989, **1**, 9811.
14 M. I. and T. Y. and Y. U. and W. K. and R. Blinc, *Sci. Technol. Adv. Mater.*, 2004, **5**, 417.
15 D. A. Tenne, A. K. Farrar, C. M. Brooks, T. Heeg, J. Schubert, H. W. Jang, C. W. Bark, C. M. Folkman, C. B. Eom and D. G. Schlom, *Appl. Phys. Lett.*, 2010, **97**, 142901.
16 A. Linz and K. Herrington, *J. Chem. Phys.*, 1958, **28**, 824–825.
17 S. M. Yang, S. J. Moon, T. H. Kim and Y. S. Kim, *Curr. Appl. Phys.*, 2014, **14**, 757–760.
18 M. Yashima and R. Ali, *Solid State Ionics*, 2009, **180**, 120–126.

19 N. Ortega, A. Kumar, O. Resto, O. A. Maslova, Y. I. Yuzyuk, J. F. Scott and R. S. Katiyar, *J. Appl. Phys.*, 2013, **114**, 104102.
20 N. Sai, B. Meyer and D. Vanderbilt, *Phys. Rev. Lett.*, 2000, **84**, 5636–5639.
21 S. H. Shah, P. D. Bristowe, A. M. Kolpak and A. M. Rappe, *J. Mater. Sci.*, 2008, **43**, 3750–3760.
22 S. M. Nakhmanson, K. M. Rabe and D. Vanderbilt, *Appl. Phys. Lett.*, 2005, **87**, 102906.
23 M. Liu, C. Ma, G. Collins, J. Liu, C. Chen, C. Dai, Y. Lin, L. Shui, F. Xiang, H. Wang, J. He, J. Jiang, E. I. Meletis and M. W. Cole, *ACS Appl. Mater. Interfaces*, 2012, **4**, 5761–5765.
24 M. Liu, C. Ma, G. Collins, J. Liu, C. Chen, A. Alemayehu, G. Subramanyam, Y. Ding, J. Chen, C. Dai, Y. Lin and M. Cole, *Nanoscale Res. Lett.*, 2013, **8**, 1–6.
25 M. Liu, J. Liu, C. Ma, G. Collins, C. Chen, A. D. Alemayehu, G. Subramanyam, J. He, J. Jiang, E. I. Meletis and A. Bhalla, *CrystEngComm*, 2013, **15**, 6641–6644.
26 S. J. Clark, M. D. Segall, C. J. Pickard, P. J. Hasnip, M. I. J. Probert, K. Refson and M. C. Payne, *Zeitschrift für Krist. - Cryst. Mater.*, 2005, **220**, 567–570.
27 H. J. Monkhorst and J. D. Pack, *Phys. Rev. B*, 1976, **13**, 5188–5192.
28 G. Kresse and D. Joubert, *Phys. Rev. B*, 1999, **59**, 1758–1775.
29 G. Kresse and J. Furthmüller, *Phys. Rev. B*, 1996, **54**, 11169–11186.
30 K. Refson, P. R. Tulip and S. J. Clark, *Phys. Rev. B*, 2006, **73**, 155114.
31 J. Junquera and P. Ghosez, *Nature*, 2003, **422**, 506–509.
32 Y.-C. Gao, C.-G. Duan, X. D. Tang, Z. G. Hu, P. Yang, Z. Zhu and J. Chu, *J. Phys. Condens. Matter*, 2013, **25**, 165901.
33 M. Zimmer, J. Junquera and P. Ghosez, *AIP Conf. Proc.*, 2002, **626**, 232–241.
34 K. Momma and F. Izumi, *J. Appl. Crystallogr.*, 2011, **44**, 1272–1276.
35 S. Piskunov, E. Heifets, R. I. Eglitis and G. Borstel, *Comput. Mater. Sci.*, 2004, **29**, 165–178.
36 E. Cockayne and B. P. Burton, *Phys. Rev. B - Condens. Matter Mater. Phys.*, 2000, **62**, 3735–3743.
37 C. Chen, T. Sasaki, R. Li, Y. Wu, Z. Lin, Y. Mori, Z. Hu, J. Wang, G. Aka, M. Yoshimura and others, *Nonlinear Optical Borate Crystals: Principals and Applications*, John Wiley & Sons, 2012.
38 S. Saha, T. P. Sinha and A. Mookerjee, *Phys. Rev. B*, 2000, **62**, 8828–8834.
39 X. D. Zhang, M. L. Guo, W. X. Li and C. L. Liu, *J. Appl. Phys.*, 2008, **103**, 063721.
40 C. Li, Z. Wang and C. Wang, *Phys. B Condens. Matter*, 2011, **406**, 2028–2032.
41 A. Tkatchenko and M. Scheffler, *Phys. Rev. Lett.*, 2009, **102**, 73005.
42 E. Moreira, C. A. Barboza, E. L. Albuquerque, U. L. Fulco, J. M. Henriques and A. I. Araújo, *J. Phys. Chem. Solids*, 2015, **77**, 85–91.
43 M. Born, *Dynamical theory of crystal lattices*, Oxford Univ. Press, 1966.
44 N. W. Ashcroft and N. D. Mermin, *Solid State Physics (Saunders College, Philadelphia, 1976)*, 2010.
45 P. Ghosez, J.-P. Michenaud and X. Gonze, *Phys. Rev. B*, 1998, **58**, 6224–6240.
46 P. Hermet, S. Goumri-Said, M. B. Kanoun and L. Henrard, *J. Phys. Chem. C*, 2009, **113**, 4997–5003.
47 S. Baroni, S. de Gironcoli, A. Dal Corso and P. Giannozzi, *Rev. Mod. Phys.*, 2001, **73**, 515–562.